The Influence of Wind and Waves on Saltwater Intrusion in the Yangtze Estuary: A Numerical Modeling Study

Zhengjin Tao[1,2,3], Yongping Chen[1,2], Shunqi Pan[3], Ao Chu[4], Chunyang Xu[1,2], Peng Yao[1,2], Samuel Rowley[3,5]

[1]The National Key Laboratory of Water Disaster Prevention, Hohai University, Nanjing 210098, China

[2]College of Harbor Coastal and Offshore Engineering, Hohai University, Nanjing 210098, China

[3]Hydro-Environmental Research Centre, School of Engineering, Cardiff University, Cardiff CF24 3AA, United Kingdom

[4]Institute of Water Science and Technology, Hohai University, Nanjing 210098, China

[5]JBA Consulting, Kings Chambers, 8 High St, Newport, NP20 1FQ, United Kingdom

Corresponding author: Yongping Chen (ypchen@hhu.edu.cn)

Key Points:

- Strong northerly winds have considerable effects on the saltwater intrusion in the Yangtze Estuary
- Combined wind and waves effects further increase the estuarine salt transport
- Wave radiation stress enhances the stratification in the North Channel under northerly winds

Abstract

Saltwater intrusion occurs frequently in the Yangtze Estuary during winter, when the river discharges are low along with strong wind and waves. However, the influence of wind and waves on saltwater intrusion in the Yangtze Estuary remains unclear. This study uses a coupled wind-wave-current numerical model based on Delft3D to investigate the impacts of wind and waves on saltwater intrusion in the Yangtze Estuary. The results show that the strong northerly wind alone enhances saltwater intrusion in the estuary by inducing a counterclockwise circulation and reducing the stratification. However, with the combined effect from wind and waves, it is found that stratification is reduced in the outer North Channel, but enhanced in the inner North Channel, which results in an increase of salt transport in the estuary by approximately 40%. The results highlight the fact that saltwater intrusion in the Yangtze Estuary could be significantly underestimated without considering waves.

Plain summary

The effect of wind on saltwater intrusion in estuaries has been widely reported, However, strong wind can generate strong waves, but relatively few studies explore the combined effect of wind and waves on saltwater intrusion. This study uses a strong wind event that occurred in the Yangtze Estuary in 2014 with a coupled computer model to demonstrate such an effect. We found that the peak salt transport can be significantly underestimated without considering waves, as they play an

important role in salt transport during strong wind events. Therefore, it is necessary to consider the combined influence from wind and waves in studying saltwater intrusion in estuaries to ensure the safety of the freshwater supply.

1 Introduction

Estuaries have always been important resources for human settlement, agriculture, transportation, and ecosystem services (Savenije, 2015). Nonetheless, saltwater intrusion can lead to a shortage of freshwater, a vital resource for people, agriculture, and fishing near estuaries. Saltwater intrusion is a typical phenomenon within estuaries, closely linked to many fundamental estuarine processes. River discharge drives freshwater out of the estuary, while tides force saltwater into estuaries and upstream through dispersion and baroclinic pressure (Monismith et al., 2002). The convergence of freshwater and saltwater in estuaries induces gravitational circulation due to the density difference (Hansen & Rattray, 1965; Pritchard, 1952), along with mixing and stratification processes (MacCready et al., 2018; Wang & Geyer, 2018). Saltwater intrusion also influences the mass transport of sediments, contaminants, nutrients and the availability of water supply (Kalhoro et al., 2021; Mai et al., 2022; Pang et al., 2010). Therefore, it is a complex process governed by multiple factors, with the river discharge and tides being regarded as the primary drivers. In general, saltwater intrusion occurs under the conditions when river discharge is low and tidal range is large (Geyer & MacCready, 2014; Prandle, 1981; Qiu et al., 2012; Xu et al., 2020). In addition, wind and waves can also have considerable effects on saltwater intrusion by modifying flow patterns, stratification, and hence salt transport.

Wind modulates the dynamics of coastal systems such as estuaries and lagoons (Giddings & MacCready, 2017; Jongbloed et al., 2022; Juárez et al., 2024). Wind effects can be broadly categorized into remote and local wind influences. Remote wind influence refers to that incurred by the alongshore and upwelling- and downwelling favorable wind in the offshore area, such as Ekman transport, generating net water transport right to the direction of the wind in the Northern Hemisphere. The Ekman transport is widely recognized as one of the key saltwater intrusion mechanisms in many estuaries (Kim & Park, 2012; Pfeiffer-Herbert et al., 2015; Ross et al., 2015), as it leads to water level setups and increases saltwater intrusion (Li et al., 2012). Within multi-inlet estuary systems such as the Yangtze Estuary, wind direction also significantly affects the horizontal residual circulation. Earlier research showed that the northerly and southerly winds generate counterclockwise and clockwise circulations in the Yangtze Estuary (Tao et al., 2020). The local wind influence refers to those incurred by the longitudinal wind along the channel inside the estuary. The local wind often affects the interaction between the wind straining and the direct wind mixing of the water column. Due to the wind straining, the up-estuary wind tends to decrease the vertical shear and circulation, while the down-estuary wind can increase the vertical shear and circulation. However, the wind mixing effect would be dominant when the wind is strong enough and destroy the vertical velocity shear and salinity stratification. (Chen & Sanford, 2009; Scully et al., 2005). Remote and local winds can affect saltwater intrusion differently. For instance, in the Delaware Bay Estuary, the remote wind causes an increase in water level and forces the saltwater landwards, while the local northwesterly wind causes a decrease of water level and forces the saltwater seawards. Taking account for remote and local wind effects allows for a more precise prediction of the salt front location (Cook et al., 2023).

In addition to winds, waves play a significant role in the estuarine hydrodynamics. Chen et al. (2019) summarized the wave effects on current into four mechanisms： Stokes drift, modulation of surface wind stress, enhanced bottom stress, and wave-induced forces. The radiation stress, which is the additional momentum flux due to waves, contributes to the wave breaking, wave setup and wave-induced currents (Longuet-Higgins & Stewart, 1964). The wave impacts on currents can be expressed in the gradient of radiation stress in the momentum equations in numerical models (Mellor, 2008). Stratification is also influenced by waves. During typhoons, for example, wave-induced mixing can destroy plume stratification and modify vertical structure (Zhang et al., 2018). In the Pearl River Estuary, wave-induced mixing has been shown to alter the river plume structure and flushing time scale (Zhang et al., 2021). Waves also have a great influence on transport processes in estuaries and coastal zones. By increasing surface drag, waves can amplify subtidal exchanges and horizontal transport (Pareja-Roman et al., 2019). In the Beibu Gulf, China, wave-enhanced bottom stresses dominate and weaken the onshore component of circulation (Yang et al., 2020). Waves not only impact hydrodynamics and salinity transport but also influence sediment transport (Zhang, et al., 2021). Waves alter the density gradient by increasing bottom shear stress and the resuspension of sediment from the bed bottom to the water column (Brand et al., 2010; Hsu et al., 2006). It has been shown recently that the density effect due to sediment concentration also further elevates saltwater intrusion (Zhu et al., 2021, 2022).

The severe saltwater intrusion event in the winter of 2014 in the Yangtze Estuary is an example of wind and wave impacts. Researchers attributed the abnormal salinity increase primarily to the remote wind-induced water level setup and Ekman transport (Zhang et al., 2019). The northerly winds drove landward water flux and transported high salinity water into the North Channel (Zhu et al., 2020). The Deep Waterway Projects, which consists of two dikes constructed in the North Passage, also played an important role (Li et al., 2020). The Intensified saltwater intrusion events have also been documented under summer typhoons, challenging the notion that saltwater intrusion hardly occurs in the wet season (Gong et al., 2018; Li et al., 2022; Wang et al., 2022). Though strong northerly winds have been noted as the dominant factor for severe saltwater intrusion events, few studies have analyzed the combined contribution of wind and waves. Especially under climate change and human activities, estuaries suffer from an increasing risk of saltwater intrusion (Lee et al., 2024). Disentangling the influence of wind and waves is critical for anticipating and managing future incidents. Therefore, this study implements a coupled wind-wave-current model based on Delft3D to quantify wind and wave effects on hydrodynamics, stratification, and transport, including water and salt.

2 Data and Methods

2.1 Study area

The Yangtze Estuary (also known as Changjiang Estuary) is the largest estuary in China, as shown in Figure 1, and it is located on the east coast of China. The Yangtze River discharges river flow through three branches and four outlets to the sea. The estuary has a complex topography with islands and shoals. Chongming Island separates the estuary into the North Branch and the South Branch, with the South Branch then divided into the North Channel and South Channel by Changxing and Hengsha Islands. The Jiuduansha Shoal further separates the South Channel into the North Passage and the South Passage towards the mouth of the estuary.

The Yangtze Estuary is a meso-tidal estuary with an abundant river discharge. The annual average tidal range at the South Channel mouth is 2.66 m, with a maximum value of 4.62 m. Datong is typically considered as the river discharge boundary of the estuary. The annual mean river discharge at the Datong station is 29300 m^3/s. Maximum discharge typically occurs during July and August each year, while the minimum discharge is usually observed between October and February. The discharge distribution throughout the year is uneven, with the flood season accounting for 72% of flows, while the dry season comprises only 28% (Wang et al., 2019). The Yangtze Estuary exhibits the characteristics of a subtropical monsoon climate, with prevailing southeast winds in summer and north winds in winter. The annual mean wind speed within the Yangtze Estuary region is 3-4 m/s and strong winds normally occur during the typhoon in summer, but strong northwesterly winds can also take place during winter. The waves in the coastal waters of the Yangtze Estuary are primarily wind waves, with wave heights and periods decreasing towards the shore. The annual mean significant wave height stands at about 0.61 m in February at the Yinshuichuan Station.

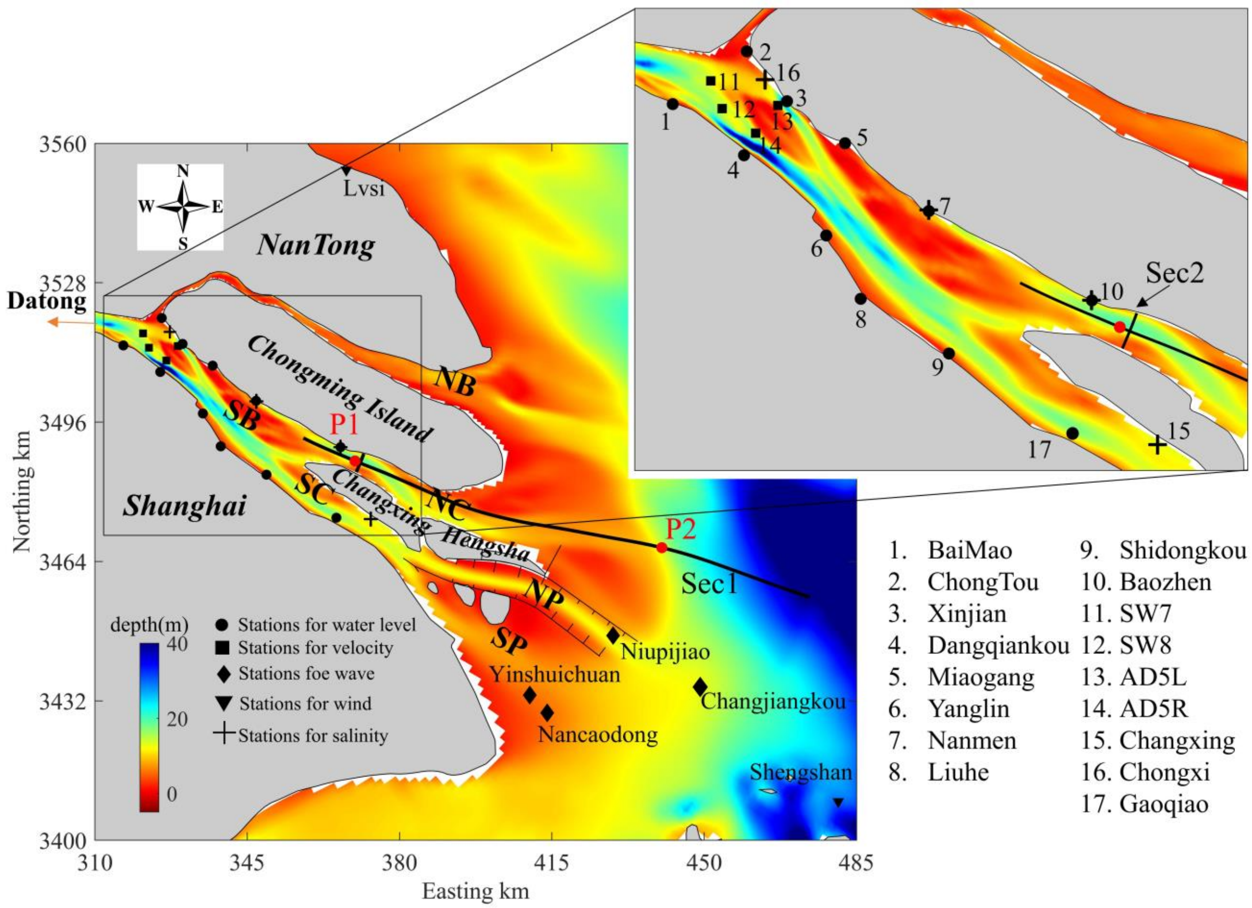

Figure 1: Topography and layout of the Yangtze Estuary. Sec1 and Sec2 are sections along and across the North Channel, respectively; P1 and P2 are locations for examining the vertical structure of current and salinity; 1-10 are stations for water level, 11-14 are stations for velocity, 10 and 15-17 are stations for salinity. NB: North Branch; SB: South Branch; NC: North Channel; SC: South Channel; NP: North Passage; SP: South Passage.

2.2 Data sets

As this study focuses on the severe saltwater intrusion event that occurred in February 2014, data of river discharge, water level, salinity, wind and waves collected during the entire February of 2014 is used. As shown in Figure 2(a), the river discharge at the Datong station during this period varied between 9875 and 13784 m^3/s, with a mean value of 11478 m^3/s, which is similar to the overall multi-year monthly mean (12430 m^3/s) for February. The minimum daily river discharge of 9875 m^3/s occurred on the 10th of February and coincided with the neap tides as indicated by the shaded strip in Figure 2(b).

The wind speed and direction at Changjiangkou station, located outside of the estuary, are shown in Figure 2(c & d). As previously reported (Dai & Zhu, 2015; Zhu et al., 2020), winds with speed exceeding 10.8 m/s as indicated by the dash line in Figure 2(c), are considered strong winds in the Yangtze Estuary. Therefore, the strong northerly wind lasted for 4.71 days and coincided with the neap tides.

Figure 2(e) shows the significant wave height H_s and wave period measured at Changjiangkou station. There is a strong correlation between wave height with wind speed in monsoon climates. The maximum wave height of 3.03 m occurred on the 7th of February 2014. Figure 2(f) shows the measured salinity at Baozhen, where a severe abnormal saltwater intrusion with a peak salinity of 20 ppt. In summary, the collected observed data indicates a saltwater intrusion in the Yangtze Estuary during the winter season, when a strong and long-lasting northerly wind co-occurs with waves.

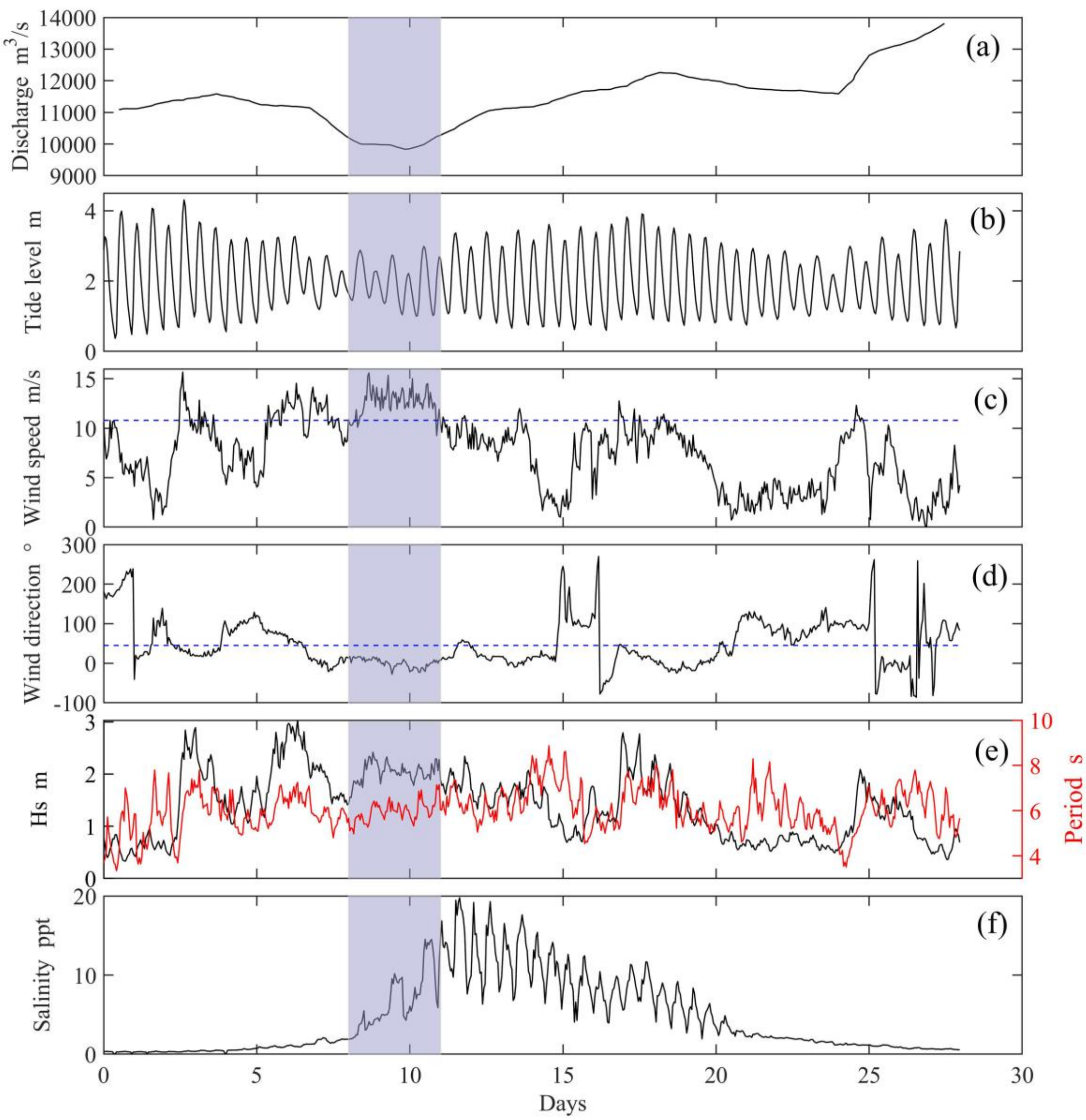

Figure 2: Time series of hourly measured data in February 2014: (a) discharge at Datong station (daily averaged); (b) tide level at Gaoqiao station; (c) - (e) wind speed, wind direction, significant wave height and period at Changjiangkou station; and (f) salinity at Baozhen station. The blue dash lines represent the wind velocity of 10.8m/s in (c) and wind direction of 45°(NE) in (d)

To better understand the severe salt intrusion event that occurred in February 2014, long-term wind data was collected from the National Marine Data Center, National Science & Technology Resource Sharing Service Platform of China (National Marine Data Center, 1999). The wind data from Lvsi and Shengshan stations for the winter seasons of 2012 to 2022 are examined. The locations of these two stations are shown in Figure 1. Lvsi is located on the northern coastline and Shengshan is located outside the Yangtze Estuary. As shown in Figure 3, the prevailing wind direction in the Yangtze Estuary is from between the northwest to northeast directions, with a directional probability of 70% throughout the winter season. The frequency of wind speeds of more than 10 m/s at Lvsi and Shengshan was approximately 12% during the decade. Despite the infrequent occurrence of strong wind events, their impact on the water supply from the Yangtze Estuary is notable. Waves are often thought to have small effects on estuarine dynamics and salt transport, which may explain the research gap on waves in the Yangtze Estuary. The average significant wave heights in February from 2016 to 2019 at Niupijiao, Nancaodong, and Changjiangkou are 0.67 m, 0.71 m, and 1.15 m, respectively. However, under strong wind conditions, as discussed in this paper regarding the 2014 intense wind event, the average wave heights at these three sites exceeded the multi-year averages, indicating intensified wave conditions. In recent years, saltwater intrusion has been observed to be enhanced during typhoon conditions (Li et al., 2022; Wang et al., 2022). Under higher runoff conditions, typhoons can still suppress large runoff volumes, leading to landward water and salt fluxes in the North Channel. Typhoons always generate waves that larger compared to normal conditions. These findings further support the importance of considering the role of wind and waves when exploring saltwater intrusion in estuaries.

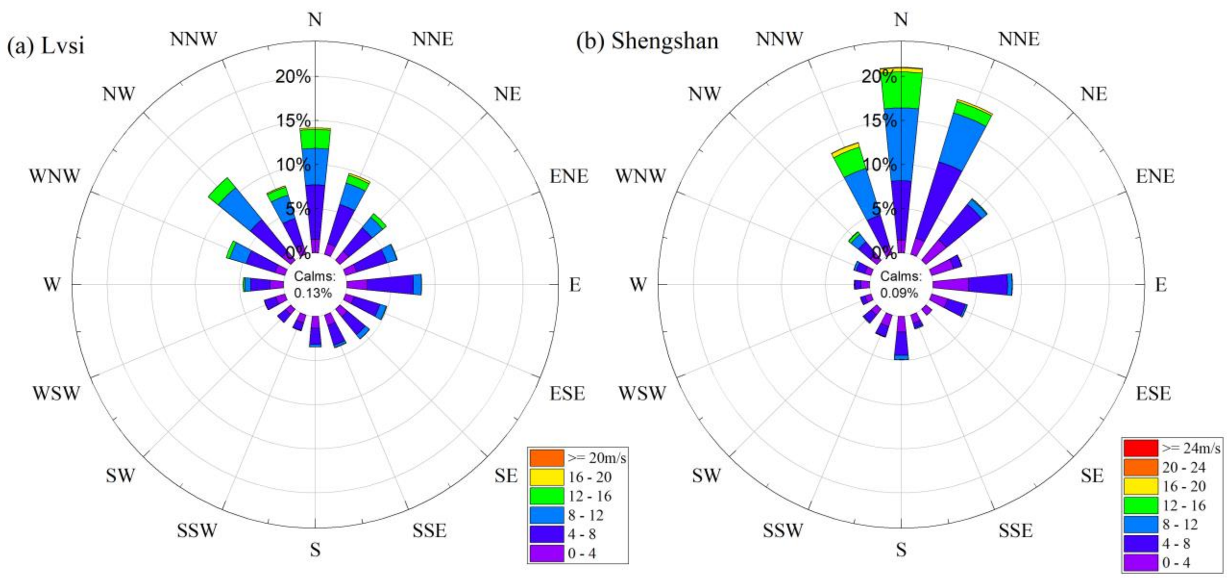

Figure 3: Wind rose polar diagrams for the period of 2012-2022 at: (a) Lvsi; and (b) Shengshan.

2.3 Numerical model

2.3.1 Model setup

To investigate the effect of wind and waves on saltwater intrusion in the Yangtze Estuary, a coupled modelling framework based on Delft3D model for flows and SWAN model for waves, which has been well calibrated and used in previous research about sediment transport, morphodynamics and saltwater intrusion (Chu, 2019; Chu et al., 2009, 2015, 2018, 2020; Zhao et al., 2023), is adopted in this study. The modelling framework, as shown in Figure 4, consists of 3 model domains: a 2D tide domain for Yangtze River and Qiantang River; a 3D tide and wave domain centered at the Yangtze Estuary; and a large wave domain to provide the wave boundary conditions to the 3D tide and wave domain, for computational efficiency. Both 2D tide domain and 3D tide and wave domain use the cantilever curvilinear grid systems, and the large wave domain uses a rectangular grid system.

The 2D tide domain has 1056 and 30 grid points in longitudinal and transverse directions respectively for the Yangtze River, with a resolution varying from 100 to 1500 m, and 137 and 6 grid points in longitudinal and transverse directions respectively for the Qiantang River, with a resolution varying from 200 to 1200 m. The 3D tide and wave domain covers the Yangtze Estuary and the adjacent coastal water over a 300 km^2 area, with its grid containing 200 node points in both easting and northing directions, and a varying resolution from 200m near the river boundary and to 6 km near the open boundary at sea. Twelve sigma layers are used in the vertical direction with the sigma levels of 0.03, 0.05, 0.08, 0.10, 0.12, 0.12, 0.12, 0.12, 0.10, 0.08, 0.05, and 0.03 from surface to bottom. This design provides a relatively higher resolution at the water surface and bottom. The wave domain (denoted as Wave in Figure 4) covers a large coastal area adjacent to the Yangtze Estuary and has a total of 62 $\times$ 78 grid points with a spatial resolution of 8000 m.

The 2D tide domain is operated with Delft3D model for both Yangtze River and Qiantang River and it is driven by river discharges and tides. The river boundary is at Datong for the Yangtze River and at Lucipu for the Qiantang River. The measured hourly river discharge data is used for Yangtze River, while the multi-year monthly average discharge is imposed for Qiantang River due to the lack of measured data.

The 3D tide and wave domain is operated with Delft3D and SWAN models. At its open boundary, tidal levels derived from the TPXO database with 13 tidal constituents (M2, S2, N2, K2, K1, O1, P1, Q1, MF, MM, M4, MS4 and MN4) are imposed. In addition, the wind-induced water level setup at the open boundary is also considered with the water level rise obtained from previous work (Zhu et al., 2020), which was calculated by subtracting the astronomical tidal level from the water level under wind. Salinity at the open boundary is derived from the long-term averaged value. Wind and atmospheric pressure data from the ERA-5 reanalysis dataset with a temporal resolution of 1 hour and a spatial resolution of 0.25 degrees is also used as surface forcing. The wind speed from ERA-5 tends to be underestimated so the observed wind data of Changjiangkou station was used to correct the reanalysis data (Li et al., 2020; Tao et al., 2022).

The large wave domain is operated with SWAN model, driven by the surface wind and atmospheric pressure from the ERA-5 reanalysis dataset. This domain is mainly to provide the wave conditions at the open boundary of the 3D tide and wave domain. Where the SWAN model is used, the processes of depth-induced breaking, wind growth, white capping, bottom friction and non-linear wave-wave interactions are all included.

Numerical simulations over the 3 model domains with Delft3D and SWAN models are fully coupled. The communication between the 2D and 3D domains takes place on the inner interfaces sharing the same grid resolution. The wave conditions along the open boundary of the 3D tide and wave domain are provided from the results of the wave domain. The model details are summarized in Table 1.

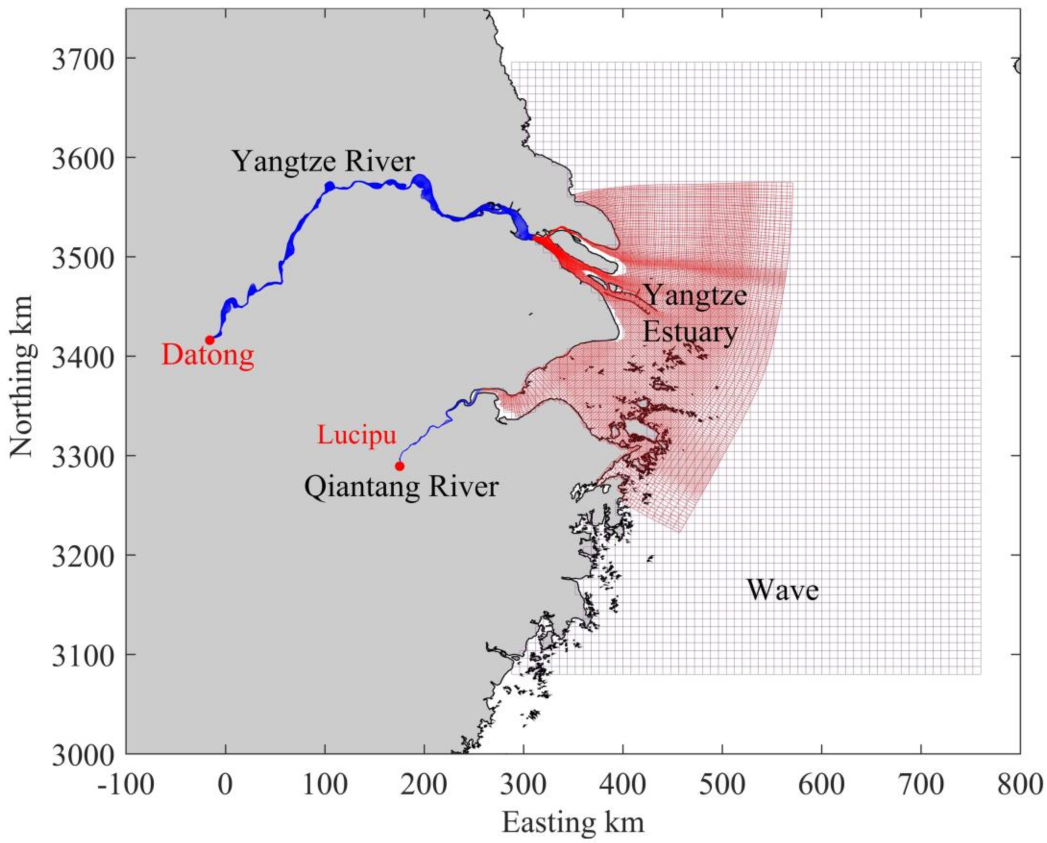

Figure 4: Model grids of the Yangtze Estuary: Blue for the 2D tidal model (Yangtze River and Qiantang River); Red for the 3D tidal and wave models (Yangtze Estuary); and Black for the wave model.

Table 1 Parameters for model domains

Parameters	Model domain			
	Yangtze River	Qiantang River	Yangtze Estuary	Wave
Grid resolution	1056×30 (0.1-1km)	137×6 (0.2-1.2km)	200×200 (0.2-6km)	62×78 (8km)
Manning coefficient (s/ $m^{1/3}$)	0.019	0.019	0.011	
Horizontal eddy viscosity (m^2/s)	2	2	2	
Horizontal eddy diffusivity (m^2/s)	50	50	0.1	
Vertical eddy viscosity (m^2/s)			0.0001	
Vertical eddy diffusivity (m^2/s)			0.00001	
Turbulence model			k-ε	
Depth-induced breaking γ				0.73
Bottom friction (m^2/s^3)				0.067
Non-linear triad interactions				on
Wind growth				on
White capping				on

The initial condition of water level and current is set as zero. The initial salinity condition is obtained by a two-years simulation with the long-term monthly-averaged river discharge. The model simulation period is from the 1st to the 24th February 2014, with the first 6 days as the leading time to ensure model stability, and the results from the subsequent period are used for the analysis. The time step of flow model is 1 min and the coupling time step between SWAN and Delft3D is 60 min.

2.3.2 Model validation

The root mean square error (RMSE), Pearson correlation coefficient (r), and the skill score (SS) (Willmott, 1981) are used to assess the model performance. They are calculated as follows:

$$RMSE = \sqrt{\frac{1}{N}\sum (X_{mod} - X_{obs})^2} \tag{1}$$

$$r = \frac{\sum \left(X_{mod} - \overline{X_{mod}}\right)\left(X_{obs} - \overline{X_{obs}}\right)}{\sqrt{\frac{1}{N}\sum \left(X_{mod} - \overline{X_{mod}}\right)^2}\sqrt{\frac{1}{N}\sum \left(X_{obs} - \overline{X_{obs}}\right)^2}} \tag{2}$$

$$SS = 1 - \frac{\sum (X_{mod} - X_{obs})^2}{\sum \left(\left|X_{mod} - \bar{X}_{obs}\right| + \left|X_{obs} - \bar{X}_{obs}\right|\right)^2} \tag{3}$$

where X is a given variable such as water level or salinity, N is the number of the data, subscript *mod* is for the model results and subscript *obs* is for the observed data. The overbar represents the time average value. For SS, the following groups are used to judge the performance of the model: SS > 0.65 indicating an excellent agreement with measured data; 0.5 < SS < 0.65 means a very good agreement with observed data; 0.2 < SS < 0.5 shows a good validation, and SS < 0.2 indicating a poor model performance.

Figure 5 shows the time series of the model results for water level, velocity, significant wave height and salinity from the 8th to the 18th February at 8 stations, in comparison with the observations.

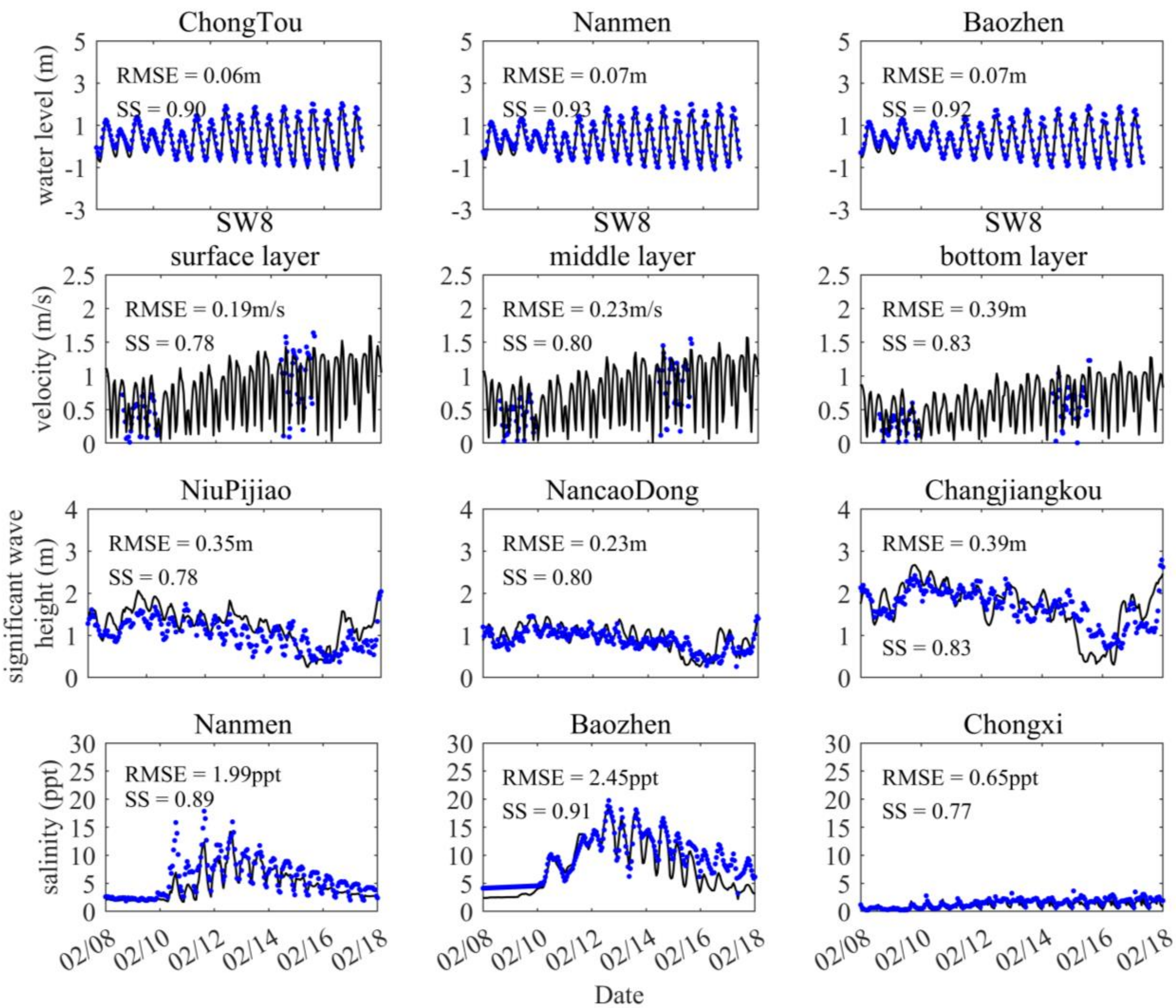

Figure 5: Comparison of observation and simulation results during February 2014 for water level, current velocity at different layers, significant wave height and salinity at selected locations

Generally, the model results are in good agreement with the measured data. With Eqs. (1, 2 & 3), RMSE, r and SS are calculated at several specific locations in the study area and listed in Table 2. From Table 2, the coupled modelling system demonstrates satisfactory performance. For water level, the RMSE is less than 0.15 m and SS over 0.9 across 9 stations. For flow velocity, the RMSE of velocity ranges from 0.19 to 0.33 m/s in the surface layer and from 0.19 to 0.29 m/s in the bottom layer, and the SS ranges from 0.81 to 0.96 in the surface layer and from 0.69 to 0.88 in the bottom layer. The significant wave heights are also well modelled with the reasonably low RMSEs from 0.23 to 0.39 m, and high SS (> 0.65). For salinity, the RMSE ranges from 0.81 to 3.6 ppt and the SS ranges from 0.68 to 0.91. The model results agree well with measurements in Nanmen, Baozhen and Changxing with skill scores above 0.8, except for Chongxi due to the complex flow patterns as it is located near the conjunction between the South Branch and the North Branch. Overall, the model performs satisfactorily in terms of reproducing the hydrodynamic parameters and salt intrusion.

Table 2 The statistical results between measured data and model results

	Station	RMSE	r	SS
Water level (m)	BaiMao	0.13	0.98	0.99
	ChongTou	0.14	0.98	0.99
	Xinjian	0.14	0.98	0.99
	Dangqiankou	0.13	0.99	0.99
	Miaogang	0.15	0.98	0.99
	Yanglin	0.13	0.98	0.99
	Nanmen	0.14	0.98	0.99
	Liuhe	0.15	0.98	0.99
	Shidongkou	0.13	0.98	0.99
	Baozhen	0.13	0.98	0.99
Surface velocity (m/s)	SW7	0.21	0.91	0.91
	SW8	0.19	0.92	0.95
	AD5L	0.27	0.88	0.90
	AD5R	0.33	0.80	0.81
Middle velocity (m/s)	SW7	0.21	0.92	0.90
	SW8	0.18	0.92	0.95
	AD5L	0.19	0.91	0.94
	AD5R	0.31	0.83	0.82
Bottom velocity (m/s)	SW7	0.28	0.90	0.69
	SW8	0.20	0.89	0.88
	AD5L	0.19	0.86	0.85
	AD5R	0.29	0.79	0.72
Significant wave height (m)	Nancaodong	0.23	0.67	0.80
	Niupijiao	0.35	0.73	0.78
	Changjiangkou	0.39	0.74	0.83
Surface salinity (ppt)	Nanmen	2.56	0.79	0.83
	Baozhen	3.60	0.82	0.85
	Chongxi	0.81	0.57	0.68
	Changxing	1.08	0.87	0.91

2.3.3 Numerical experiments

To investigate the wind and wave-induced changes in hydrodynamics and salinity transport, three model cases are considered in this study for numerical experiments to include tides, river discharges, waves and winds respectively. Case 1 is the baseline case with tides and river discharge included, Case 2 includes wind in addition to the conditions of Case 1, and Case 3 includes waves on the conditions of Case 2, as summarized in Table 3. Those model configurations allow inter-comparisons to be carried out to clearly identify the effect of wind and waves on saltwater intrusion at the study site.

Table 3 Cases for numerical experiments

Case	Tide	River discharge	Wind	Wave
1	√	√		
2	√	√	√	
3	√	√	√	√

To describe the water and salt transport in the Yangtze Estuary, the net water flux per unit width q_w and the net salt flux per unit width q_s are introduced and calculated as follows (Lu Li et al., 2012; Linjiang Li et al., 2022):

$$q_w = \left\langle \int_{-1}^{0} (h+\xi) u d\sigma \right\rangle \qquad (4)$$

$$q_s = \left\langle \int_{-1}^{0} (h+\xi) us d\sigma \right\rangle \qquad (5)$$

where < > denotes the time average defined as $< ... > = \frac{1}{T}\int_0^T ...dt$, h is the water depth, ξ is the water surface level, *u and s* are the instantaneous current and salinity, σ is the relative water depth with -1 being at the bottom and 0 at the surface, and T is the period over which the quantity is averaged. Similarly, the net cross-sectionally integrated water flux F_w and salt flux F_s are defined as follows:

$$F_w = \left\langle \int_0^L \int_{-1}^{0} (h+\xi) u d\sigma dy \right\rangle \qquad (6)$$

$$F_s = \left\langle \int_0^L \int_{-1}^{0} (h+\xi) us d\sigma dy \right\rangle \qquad (7)$$

where L is the width of the cross-section, u is the velocity component perpendicular to the section, and s is the salinity.

To understand the mechanism of salt transport, the velocity is decomposed into spatially and temporally averaged current velocity u_0, temporally averaged current velocity u_e, and tide current velocity u_t. Herein, u_0 represents the residual velocity. u_e varies in the vertical direction, reflecting the vertical flow structure under the influence of the density gradient. u_t changes spatially and temporally. They can be calculated as follows (Lerczak et al., 2006):

$$u_0(t) = \frac{1}{A_0} \left\langle \int_0^L \int_{-1}^{0} (h+\xi) u d\sigma dy \right\rangle \qquad (8)$$

$$u_e(t,y,\sigma) = \frac{\langle u(t,y,\sigma) dA \rangle}{\langle dA \rangle} - u_0(t) \qquad (9)$$

$$u_t(t,y,\sigma) = u(t,y,\sigma) - u_0(t) - u_e(t,y,\sigma) \qquad (10)$$

where A_0 is the low-passed area of the cross-section, and dA is the differential of the cross-sectional area. The salinity is also decomposed into three terms (s_0, s_e, and s_t) by replacing u with s. The total salt flux is decomposed as follows:

$$\begin{aligned} F_s &= \left\langle \int_0^L \int_{-1}^0 (h+\xi) us d\sigma dy \right\rangle \\ &= \left\langle \int_0^L \int_{-1}^0 (h+\xi)\left(u_0+u_e+u_t\right)\left(s_0+s_e+s_t\right) d\sigma dy \right\rangle \\ &\approx \left\langle \int_0^L \int_{-1}^0 (h+\xi)\left(u_0 s_0+u_e s_e+u_t s_t\right) d\sigma dy \right\rangle \\ &= F_0+F_e+F_t \end{aligned} \qquad (11)$$

In Eq. (11), F_0 is the advective transport, which is cross-sectionally subtidal salt transport caused by river discharge, wind-induced flows, or wave-induced flows; F_e is the shear transport resulting from the estuarine circulation; and F_t is the tidal oscillatory transport due to the temporal correlation between u_t and s_t.

To investigate the mechanisms of wind and wave effects, an examination of each term in the momentum equation is conducted for three cases. The depth-averaged momentum balance equations are written as follows (Zhang et al., 2021):

$$\begin{aligned} \frac{\partial u}{\partial t} &= -g\frac{\partial \eta}{\partial x} - \frac{gh}{\rho}\frac{\partial \rho}{\partial x} + fv - \left(\frac{\partial uu}{\partial x} + \frac{\partial vu}{\partial y}\right) + \frac{1}{h\rho}\left(\tau_s^x - \tau_b^x + \frac{\partial S_{xx}}{\partial x} + \frac{\partial S_{xy}}{\partial y}\right) \\ \underbrace{\frac{\partial v}{\partial t}}_{ACC} &= \underbrace{-g\frac{\partial \eta}{\partial y}}_{BTP} \underbrace{-\frac{gh}{\rho}\frac{\partial \rho}{\partial y}}_{BCP} \underbrace{-fu}_{COR} \underbrace{-\left(\frac{\partial vu}{\partial x} + \frac{\partial vv}{\partial y}\right)}_{ADV} + \frac{1}{h\rho}\left(\underbrace{\tau_s^y}_{WND} \underbrace{-\tau_b^y}_{BSS} + \underbrace{\frac{\partial S_{yx}}{\partial x} + \frac{\partial S_{yy}}{\partial y}}_{WAV}\right) \end{aligned} \qquad (12)$$

where u and v are the components of the horizontal velocity, η is the water level, h is the water depth, ρ is the depth-averaged density, and A_v is the vertical eddy viscosity. τ_s and τ_b are the surface stress and bed shear stress, respectively, and S_{xx}, S_{xy}, S_{yx}, and S_{yy} are the wave radiation stresses. The terms in Eq. (12) are the local acceleration (ACC), the barotropic (BTP) and baroclinic pressure (BCP) gradient, Coriolis force (COR), horizontal advection (ADV), surface wind stress (WND), bottom shear stress (BSS), and wave-induced forces (WAV).

3 Results and discussion

3.1 Effects of wind and wave on water level, water flux, salt flux and salinity

A period of three days during the neap tides (8^{th} to 11^{th} of February 2014, as indicated by the shaded strip in Figure 2) is chosen as a time window for detailed analysis. Here three days are chosen as the filter window as the M_2 is responsible for the most tidal energy in the Yangtze Estuary. The study of Wu (2010) indicated that averaging over six M_2 periods can reduce the relative error of residual transport to less than 0.03. Figure 6 shows the distributions of the three-day averages of water level, surface salinity, unit width net water flux (q_w), and unit width net salt flux (q_s) for Case 1 (the baseline case). The residual water level over the period is higher inside the estuary and decreases further offshore, with a value of 0.2 m near the North Channel mouth. Due to the stronger tide-induced landward Stokes transport (Wu, 2010), the saltwater intrusion is the strongest in the South Passage, where surface salinity is over 20 ppt. The saltwater intrusion is weakest in the North Channel, with surface salinity below 2ppt. The water flux is seaward in the South Branch, North Channel and South Channel for Case 1, while it flows into the estuary in the North Branch. A maximum water flux is 4 m^2/s in the North Channel, indicating that the North Channel is the freshwater export conduit. The salt flux has a similar distribution to the water flux. As shown in Figure 6 (d), the salt flux is much larger outside the estuary due to the higher salinity. Although the water flux in the North Channel is large, there is a little salt flux due to the low salinity.

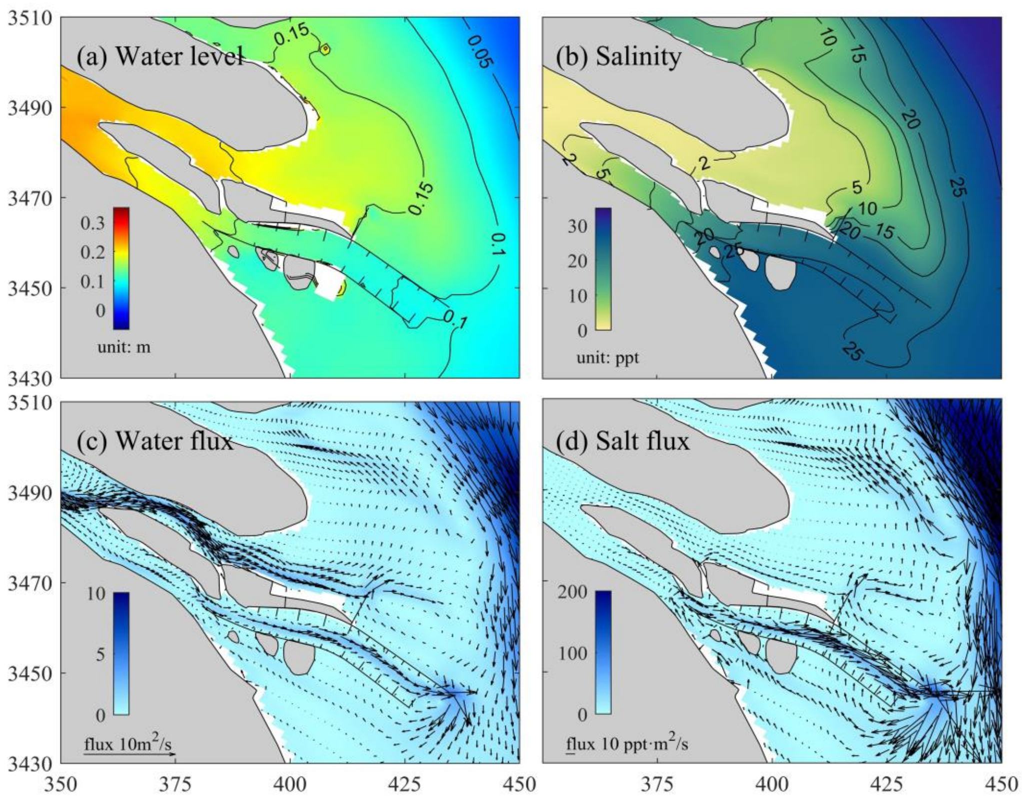

Figure 6: Distributions of 3-day averaged: (a) water level; (b) surface salinity; (c) water flux per unit width; and (d) salt flux per unit width during neap tides in February 2014

The differences of water level, salinity, net water and salt flux per unit width between Cases 1 and 2 are shown in Figure 7. When the wind effects are included (Case 2), the strong northerly wind can cause a rise of about 10 cm in the residual water level near the North Channel mouth and the water level setup decreases upstream as shown in Figure 7(a). The freshwater is transported seawards through the South Channel rather than the North Channel. Surface salinity in the South Channel decreases by about 15 ppt, but in the North Channel it increases by about 10 ppt. Water and salt flux near the North Channel mouth changes to southward under the wind effects, as shown in Figures 7(c & d). The northern dike of the Deep Waterway Project obstructs the water and salt flux and causes a division into landward and seaward transports. The wind-induced water and salt flux in the North Channel are landward with a value of about 6 m^3/s and 40 $ppt{\cdot}m^3/s$, respectively. The strong northerly wind induces a horizontal circulation into the North Channel and out of the

South Channel, as reported similarly in previous studies (Li et al., 2012; Tao et al., 2020; Zhu et al., 2020). Higher salinity water flows into the estuary under the counterclockwise horizontal circulation, leading to severe saltwater intrusion.

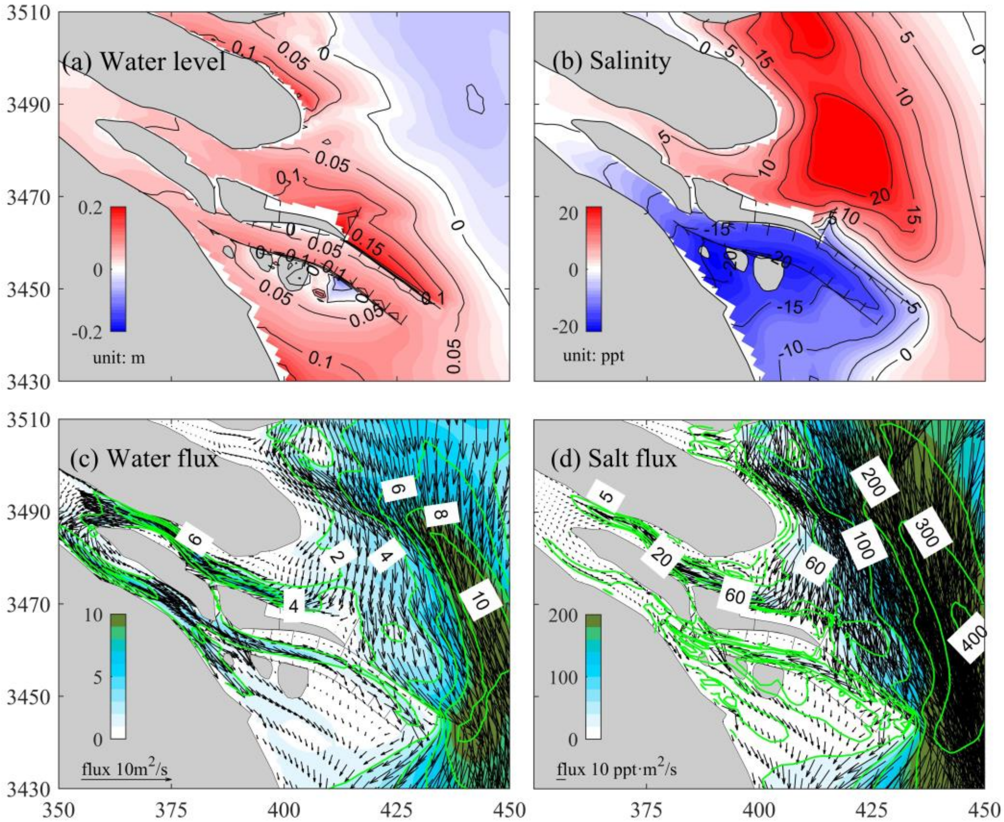

Figure 7: Differences of time-averaged: (a) water level; (b) surface salinity; (c) water flux; and (d) salt flux between Cases 1 and 2

The time-averaged significant wave height and direction, and the distribution of differences in the water level, salinity, net water and salt flux per unit width between Cases 2 and 3 is shown in Figure 8. The wave height is over 2 m outside the estuary. It decreases landward and is lower than 0.5 m upstream of the North Channel. As can be seen in Figure 8 (b), the waves cause about 1-2 cm of water level setup in the Yangtze Estuary. Figure 8 (c) shows that the surface salinity in the North Channel increases, especially in the mouth of the estuary, with a value of more than 2 ppt, indicating that the saltwater intrusion is further enhanced by the wave effect. Under the combined effects of wind and waves, the water and salt flux direction in the estuary does not change. However, the magnitude has increased. The landward wave radiation stress gradient causes the landward wave-induced water flux in the North Channel as in Figure 8 (d). Meanwhile, due to the narrowing topography in the mouth of the North Channel, the wave-induced water transport inside the estuary is larger than offshore, further enhancing the wind-driven horizontal circulation.

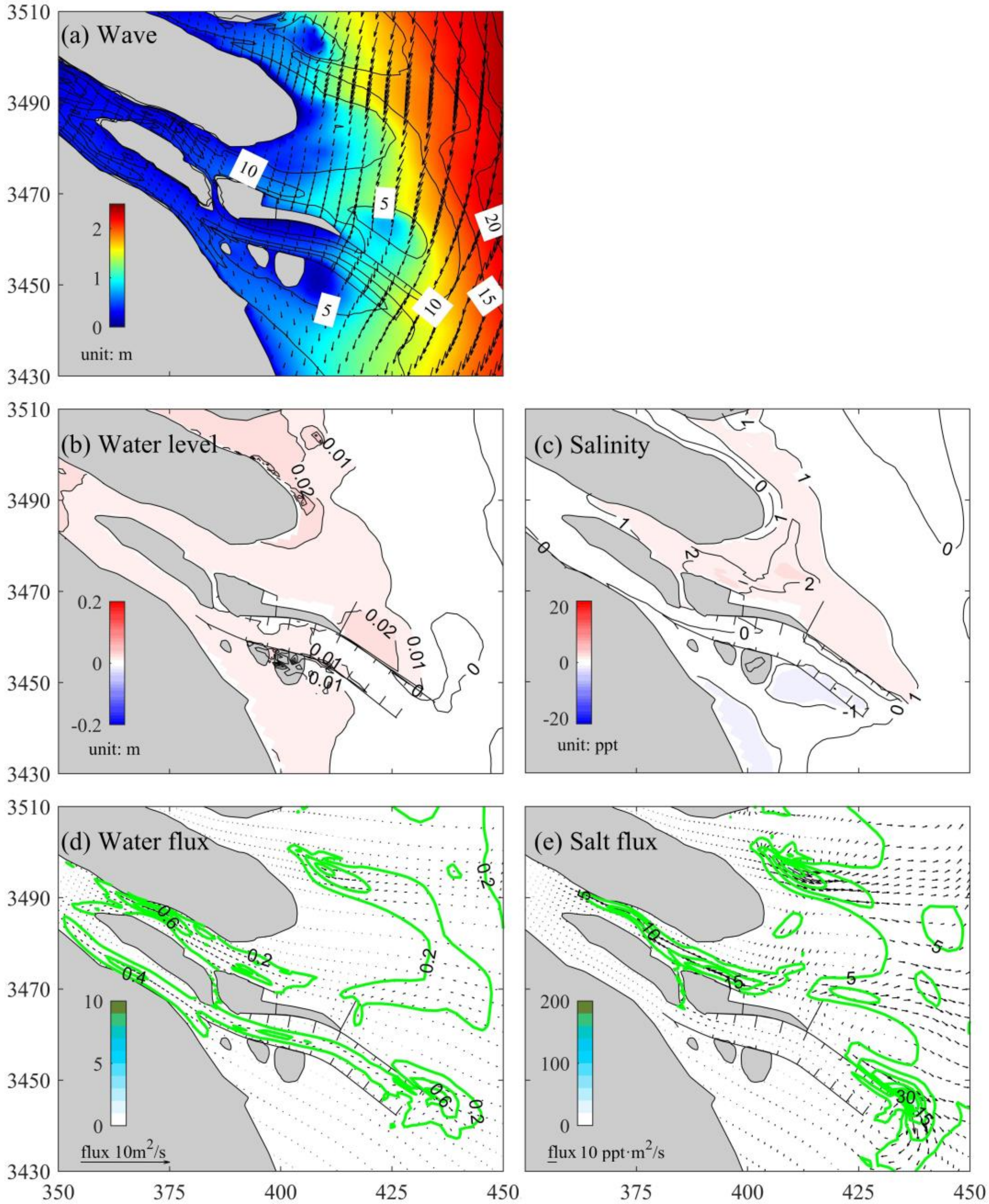

Figure 8: (a) Distributions of significant wave height and direction (contour lines denote the water depth), and differences of time-averaged: (c) water level; (d) surface salinity; (e) water flux; and (f) salt flux between Cases 2 and 3

3.2 Effects of wind and waves on vertical distributions of current and salinity

The velocity and salinity vertical profiles at two designated points, P1 which is located inside of the North Channel and P2 which is located offshore area, are investigated here. Figure 9 shows the vertical structure of current and salinity at P1 with tidally averaged, flood phase averaged, and ebb phase averaged values.

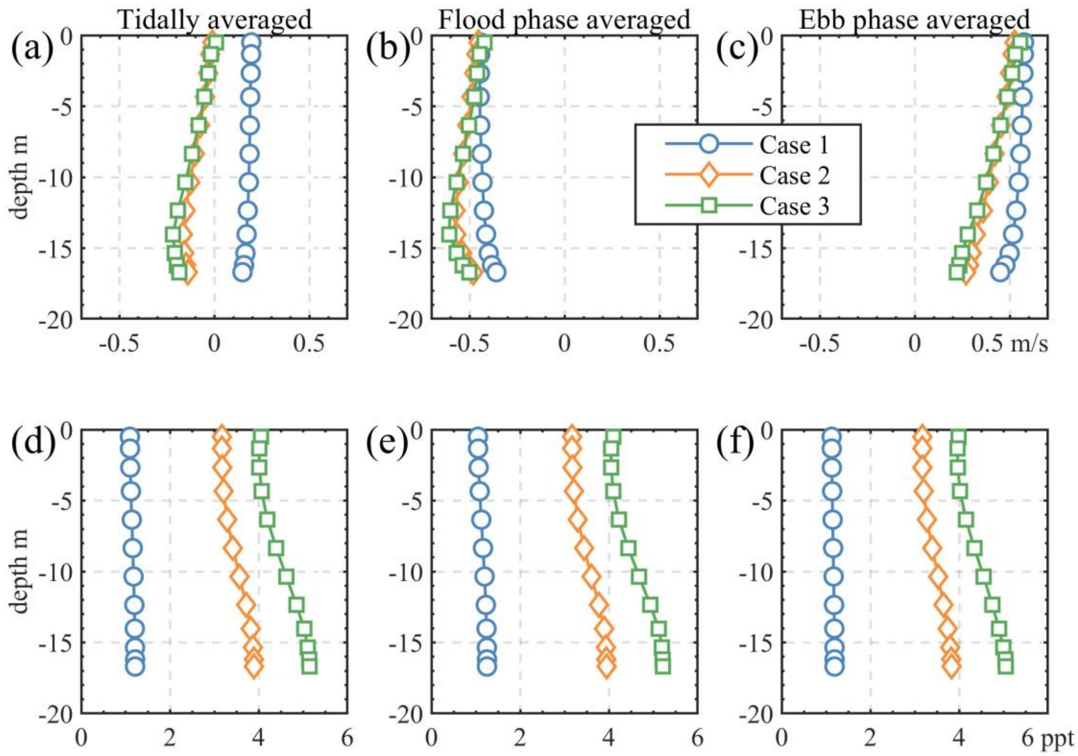

Figure 9: Vertical profiles of tidally, flood phase, and ebb phase averaged velocity (a-c) and salinity (d-f) at P1 (inside the estuary)

For the tidally averaged velocity profile, the surface velocities as shown in Figure 9(a) surpass those at the bottom. Wind causes a notable modification in the tidally averaged velocity, which changes from 0.15 m/s in Case 1 to -0.1 m/s in Case 2, i.e., from seawards flow to landwards flow. This indicates an inland residual flow in the upper North Channel. Figures 9(b & c) show that the flood tide velocity increases under the wind effect, while ebb tide velocity decreases. The most significant variations occur in the lower water column, at approximately 0.16 and -0.18 m/s, respectively. Concurrently, the vertical shear increases and the velocity difference between surface and bottom increasing from 0.04 to 0.11 m/s. Under the effects of wind and waves in Case 3. There is an increase in the flood tide velocity from 0.57 to 0.61 m/s at the bottom layer and a marginal decrease from 0.45 to 0.42 m/s at the surface layer. Figure 9(c) also shows an increase in the ebb tide velocity from 0.25 to 0.30 m/s at the bottom layer and a marginal decrease from 0.55 to 0.53 m/s at the surface layer. Nevertheless, the depth-averaged flood tide velocity increases while the depth-averaged ebb tide velocity decreases, resulting in greater saltwater intrusion into the North Channel. In addition, wave-induced transport increases the vertical shear by 55%.

Figure 9(d) depicts wind-induced vertical shear contributing significantly to water stratification. Bottom salinity exhibits an elevation from 1.2 to 3.6 ppt and the obvious vertical salinity gradient occurs under the wind effect. Under the wind and wave effects, salinity increases from the surface to the bottom with a value of approximately 1 ppt and the vertical salinity gradient is steeper.

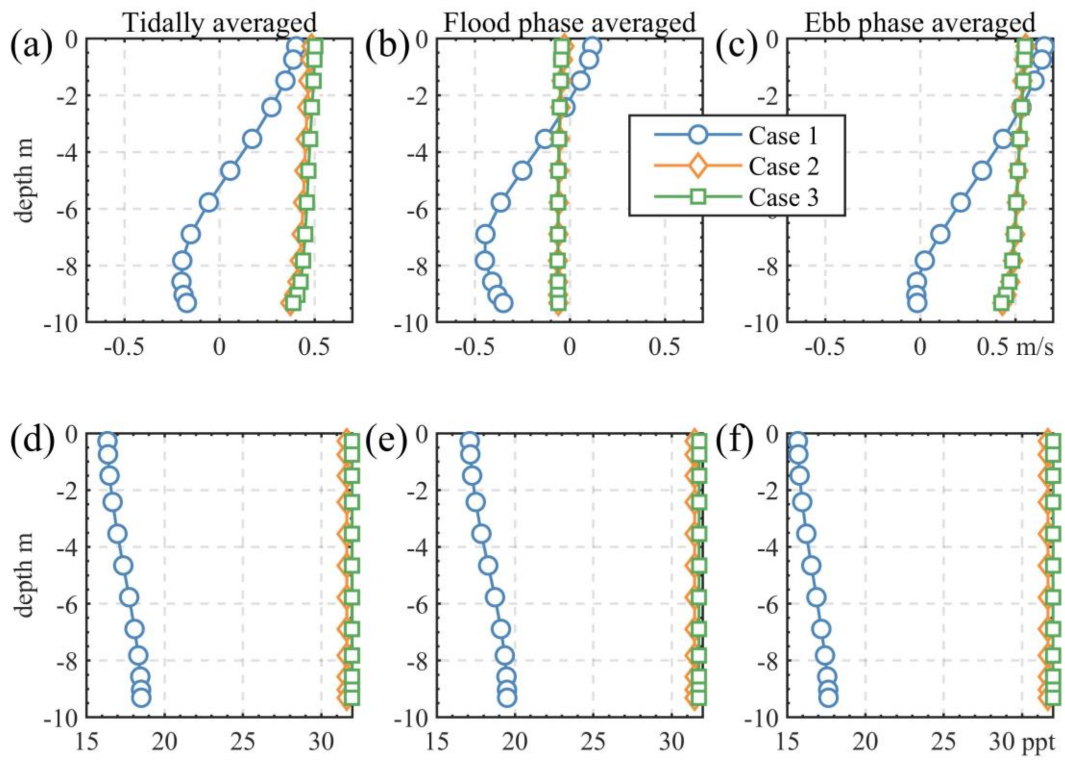

Figure 10: Same as Figure 9, but at P2 (outside the estuary)

At P2, an offshore location, the influence of wind and waves on the tidally averaged velocity and salinity profiles exhibits distinct patterns. As can be seen in Figure 10(a), the tidally averaged velocity at P2 in Case 1 indicates a landward flow at the bottom and seaward flow at the surface, but in Cases 2 and 3, the velocity profiles tend to be more constant within the water column. Figures 10(b & c) show that Ekman transport reduces ebb currents and increases flood currents at the surface, reducing the vertical shear. Simultaneously, stratification is noticeably disrupted by wind and waves, showing characteristics of vertical homogeneity as shown in Figure 10(d). The impacts of waves are found to be much smaller than that of wind, particularly in the offshore region from the estuary.

Figure 11 shows the tidally averaged distribution of the depth-averaged momentum terms along the North Channel (Sec1 shown in Figure 1) over 8-11 February for the three cases. For Case 1, which is the baseline case without wind and wave effects, Figure 11(a) shows that the time-averaged momentum balance in the areas outside the estuary is primarily determined by the Coriolis force, barotropic and baroclinic pressure gradient forces, whilst in the North Channel, it is predominantly influenced by the barotropic pressure gradient force and horizontal advection. Due to the low extent of saltwater intrusion, the water outside the estuary is highly stratified. As a result, the barotropic pressure gradient force is primarily counterbalanced by the baroclinic pressure gradient force and the Coriolis force offshore.

For Case 2, which includes the wind effect only, Figure 11(b) shows that the direction of surface wind stress is southward along the North Channel with a maximum value near the mouth. The wind blows the water from the north, inducing up-estuary Ekman transport and piling water at the north dike of the Deep Waterway Project. The barotropic pressure gradient force points northward at the mouth and it has a landward component inside the North Channel. Because currents and salinity are vertically homogeneous, the baroclinic pressure decreases offshore. The intense saltwater intrusion pushes the salinity front toward the estuary interior, causing an increase in the baroclinic pressure in the upper North Channel. The Coriolis force also shifts landward due to the influence of Ekman transport, intensifying the acceleration during the flood tide.

For Case 3, Figure 11(c) shows the time-averaged momentum balance with both wind effect and wave effect. To illustrate the wave effects more clearly, the difference between Cases 2 and 3 is demonstrated in Figure 11(d). It indicates that bottom stress increases under the combined effect of wind and waves. The landward barotropic pressure gradient force increases. This increment contributes to an increased flood tide velocity and a decreased ebb tide velocity. As shown in Figure 8(a), the southward wind stress produces the wave propagates to the south. However, the wave-induced force deviates from the direction of wind stress with a landward component. While wind waves are expected to propagate southward with the wind, bathymetric refraction at the North Channel mouth and the northern dike of the Deep Waterway Project redirects the waves onshore. The magnitude of the wave-induced force is relatively limited compared to the other forces. Yet, it aligns the acceleration more closely with the channel, consequently intensifying the landward current.

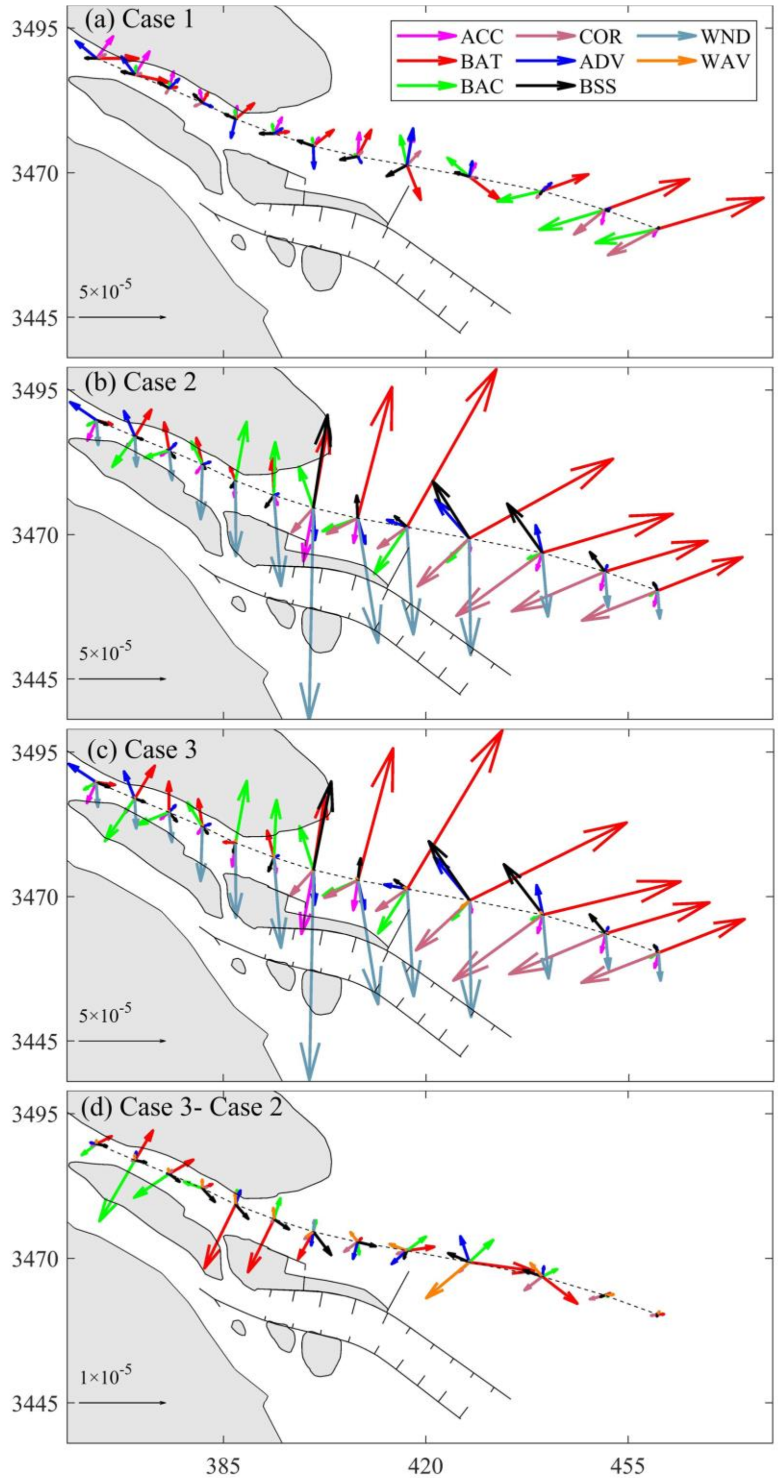

Figure 11: Snapshots of depth-averaged momentum terms: acceleration (ACC); barotropic pressure (BAT); baroclinic pressure (BAC); Coriolis force (COR); horizontal advection (ADV); bottom stress (BSS); wind stress (WND); and wave force (WAV) along the North Channel for Cases 1-3 (a-c). unit: m/s^2

3.3 Effects of wind and waves on stratification and mixing

The effects of wind and waves on water mixing and stratification are investigated by the potential energy anomaly parameter (Simpson et al., 1990). The parameter ϕ (J/m^3) is defined as $\phi = \frac{1}{h}\int_{-H}^{\eta}(\bar{\rho} - \rho) gzdz$, where h is the water depth, ρ is the water density at the depth z, $\bar{\rho}$ is the vertically averaged density, and g is the gravitational acceleration. $\phi < 10$ J/m^3 indicates complete water mixing, while $\phi > 180$ J/m^3 represents acute density difference in the vertical direction with high stratification. The potential energy anomaly parameter in three cases is shown in Figure 12.

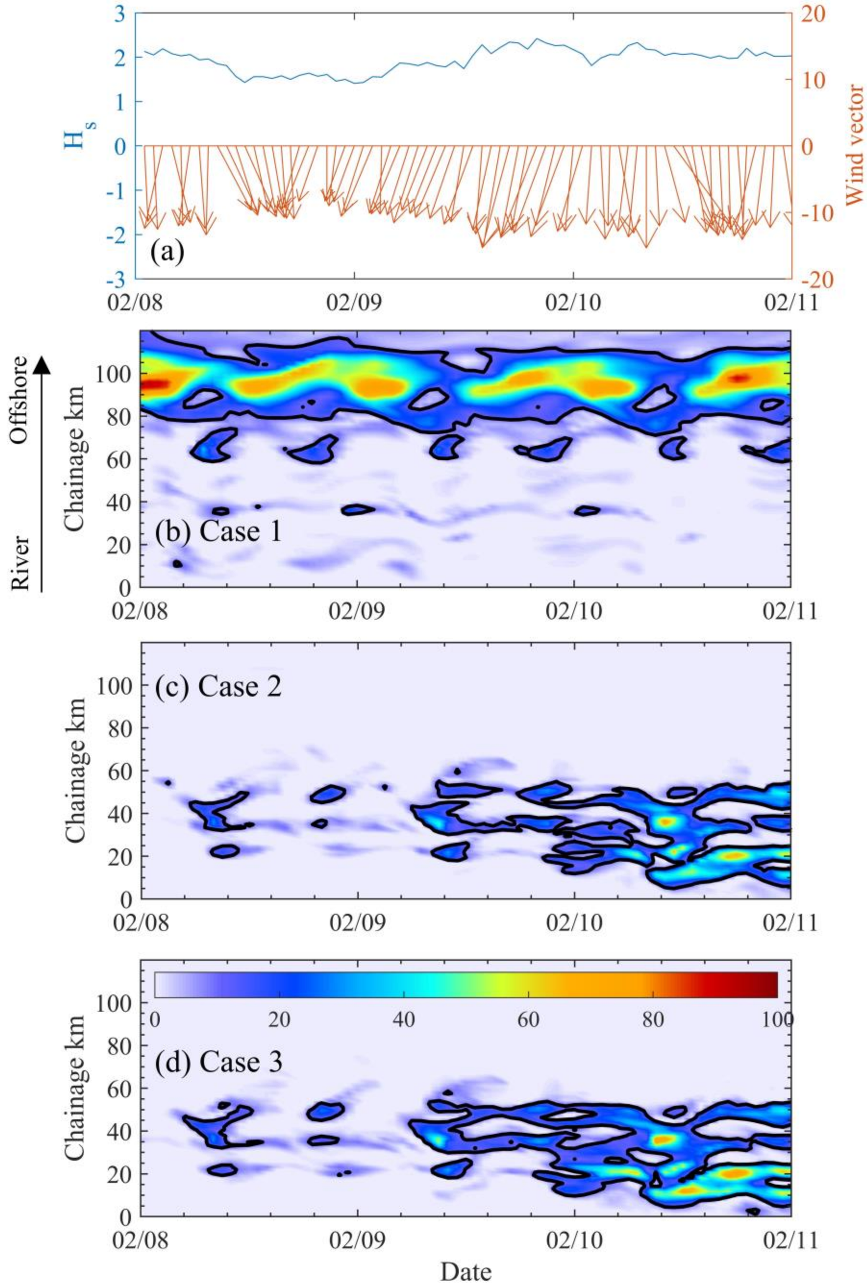

Figure 12: Spatio-temporal distributions of the low-pass filtered potential energy anomaly ϕ along Sec1: (b) Case 1; (c) Case 2; and (d) Case 3, together with (a) significant wave height and wind vectors

In the absence of wind and wave effects, ϕ at the North Channel mouth surpasses 10, while ϕ within the North Channel is lower. The North Channel is well mixed, primarily governed by river discharge, as noted in previous research (Wang et al., 2022). Figure 12(c) shows that winds reduce the potential energy anomaly offshore. The counterclockwise wind-induced circulation facilitates salt intrusion and increases stratification in the North Channel. With waves, stratification increases in the upper North Channel and slightly decreases in the lower part.3.4 Effects of wind and waves on water and salt transport

Figure 13 shows the water flux and salt flux through the upper North Channel. The water flux is always positive (seawards) in Case1 around 10000 m^3/s. However, when the effect of wind is included, a continuous reduction in the water flux cross the North Channel is observed in Case 2, turning negative (landwards) around 7.2 days, with the direction changing from seaward to landward. It reaches a maximum value of -9561 m^3/s at 9.3 days. The landwards water flux induced by the northerly wind significantly exceeds the river discharge, diverting the river discharge to the South Channel. After the 10th day, the water flux gradually decreases and returns to the conditions without wind. Accounting for the landward wave-induced radiation stress gradient, the duration of the landward water flux prolongs by 0.5 days in Case 3, with the peak value changing to -11017 m^3/s.

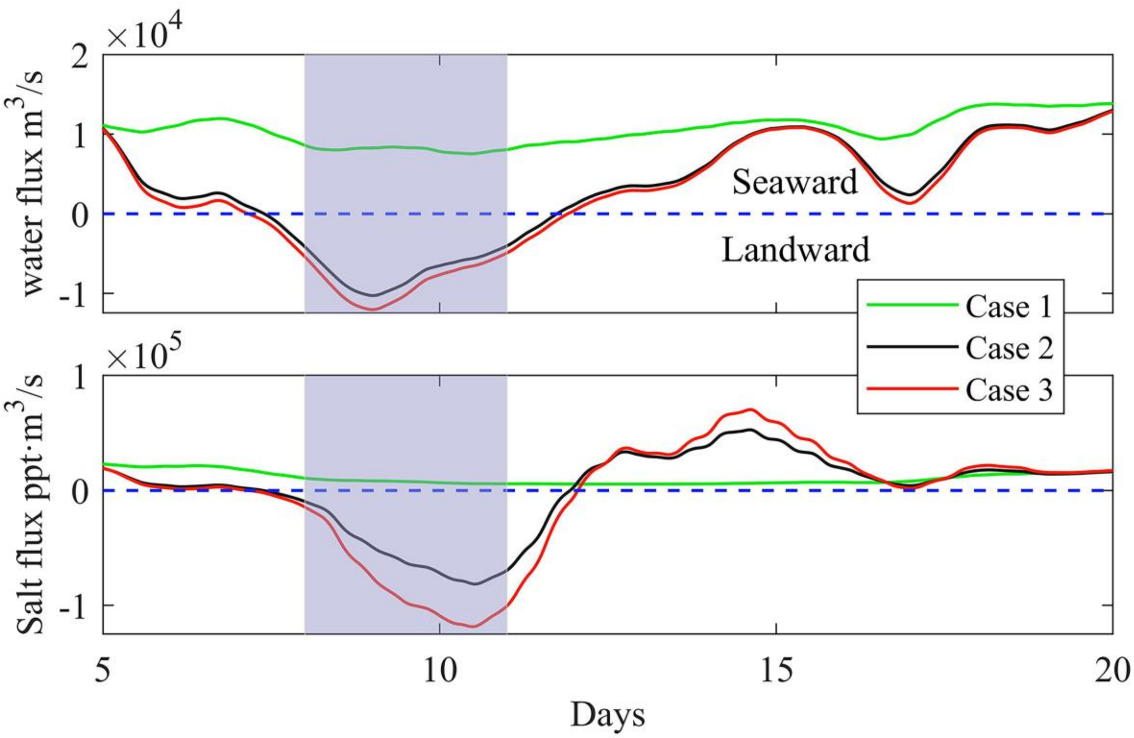

Figure 13: Time series of low-pass filtered: (a) water; and (b) salt flux through Sec2

The variation of salt flux follows a similar pattern to that of water flux. Figure 13(b) shows that the salt flux in Case1 is consistently positive, indicating a seaward transport of salinity. However, the salt flux also decreases and turns landwards around 7.2 days considering the influence of wind, as the water flux shifts toward the estuary. The peak salt flux (-83,642 ppt·m^3/s) occurs slightly later than the peak water flux. By 11.9 days, the landward salt flux diminishes to zero, and salinity reverses outward. When considering the impact of waves, the landward peak salt flux increases by about 46% (-122,175 ppt·m^3/s).

The mechanisms behind this change in water and salt fluxes are explored based on the results of the flux decomposition shown in Eq (10). As illustrated in Figure 14, the dominant mechanism governing salinity transport in cross-channel section is advection transport, regardless of the presence of wind and wave effects. Shear transport arises from vertical variations in velocity and salinity. Its direction is landwards, thereby promoting saltwater intrusion. The tidal oscillation transport is low about 10% of the total transport.

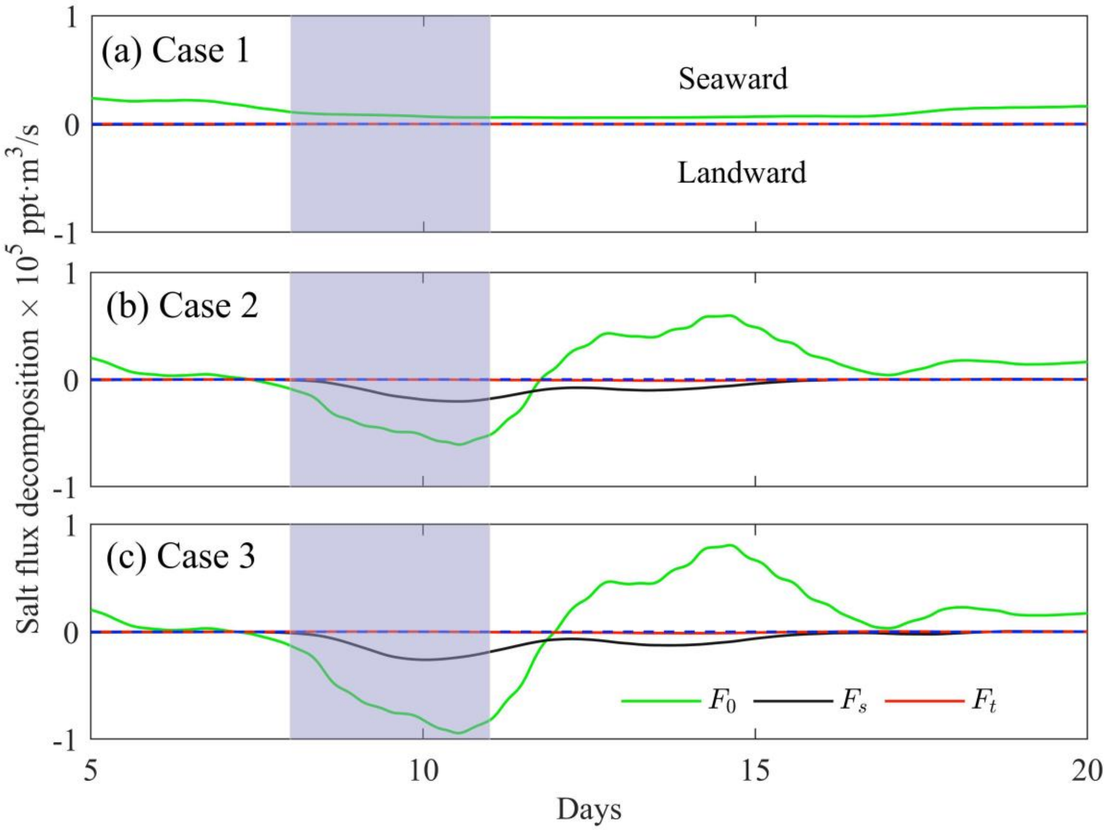

Figure 14: Time series of the advective transport F_0, shear transport F_e, and tidal oscillatory transport F_t for Cases 1-3.

4 Conclusions

This study investigates the effects of wind and waves on saltwater intrusion in the Yangtze Estuary using a coupled wind-wave-current numerical model. The effects of wind and waves are explored by examining changes in momentum, stratification, and salt transport between cases with and without the consideration of wind and waves.

The impact of wind and waves on saltwater intrusion in the Yangtze Estuary can be primarily delineated into two aspects.

1. The adjustment of momentum due to wind stress and wave radiation stress gradient generates a counterclockwise horizontal circulation. Strong northerly wind blows water to the south and generate up-estuary Ekman transport. It contributes to a localized water level rise at the Deep Waterway Project and the North Channel mouth, inducing horizontal circulation from the North Channel to the South Channel. The radiation stress gradient from refracted waves at the mouth augments the counterclockwise circulation, slightly increasing the up-estuary transport. The combined effects of wind- and wave-induced circulation on the saltwater intrusion constitutes the predominant mechanism, which is reflected in advective transport and contribute approximately 70% of the total salt transport.

2. Wind and waves influence the stratification of estuarine water, thereby affecting salinity transport in the Yangtze Estuary. Strong winds fully mix the water column offshore. In the North Channel, winds increase vertical shear and stratification, and waves also enhance the stratification. However, the wind effects are dominant and wave effects are marginal.

Overall, the influence of wind on the salt transport surpasses that of waves, though the latter impact is still noteworthy. Accounting for waves would increase the landward salt flux by around 40%. It is demonstrated that both winds and waves play integral roles in driving saltwater intrusion. This has a significant implication for predictive modelling and engineering controls on regional water quality and resources as simulating only tidal and fluvial processes could impose risks of overlooking dominant meteorological triggers leading to severe saltwater intrusion. Integrating wave and wind dynamics is therefore essential and important to achieve sufficient model accuracy. The findings from this study are applicable to other estuary systems and emphasize the key role of wind and waves in estuarine dynamics to improve the management of estuarine reservoirs.

Acknowledgments

This work is partly supported by the National Key Research and Development Program of China (No.2023YFC3008100) and the Fundamental Research Funds for the Central Universities (B230201047). ZT would like to thank the financial support from the China Scholarship Council (CSC) under the PhD exchange program (No.20220671007) and SR would like to acknowledge the support of the WISE CDT and JBA consulting in this work.

Open Research

The observed wind data at Lvsi and Shengshan can be found at National Marine Data Center, National Science & Technology Resource Sharing Service Platform of China (National Marine Data Center, 1999) (https://mds.nmdis.org.cn/pages/dataViewDetail.html?dataSetId=4). The wind and atmospheric pressure data used in the model were obtained from the ERA5 global reanalysis datasets in the Copernicus Climate Data Store (Hersbach et al., 2018) (https://cds.climate.copernicus.eu/doi/10.24381/cds.adbb2d47). The data related to this article are available online (https://figshare.com/articles/dataset/____/25309039)

References

Brand, A., Lacy, J. R., Hsu, K., Hoover, D., Gladding, S., & Stacey, M. T. (2010). Wind-enhanced resuspension in the shallow waters of south san francisco bay: mechanisms and potential implications for cohesive sediment transport. *Journal of Geophysical Research: Oceans*, *115*(C11), 2010JC006172. https://doi.org/10.1029/2010JC006172

Chen, S.-N., & Sanford, L. P. (2009). Axial wind effects on stratification and longitudinal salt transport in an idealized, partially mixed estuary*. *Journal of Physical Oceanography*, *39*(8), 1905–1920. https://doi.org/10.1175/2009JPO4016.1

Chen, Y., Chen, L., Zhang, H., & Gong, W. (2019). Effects of wave-current interaction on the Pearl River Estuary during Typhoon Hato. *Estuarine, Coastal and Shelf Science*, *228*, 106364. https://doi.org/10.1016/j.ecss.2019.106364

Chu, A. (2019). *Analysis and modelling of morphodynamics of the yangtze estuary* (Dissertation (TU delft)). Delft University of Technology. https://doi.org/10.4233/UUID:068A1257-DFC2-4389-964E-F665AA5CB213

Chu, A., Wang, Z. B., & Vriend, H. J. de. (2009). Process-based modeling for the yangtze estuary. In *Proceedings of Coastal Dynamics 2009* (pp. 1–13). Tokyo, Japan: WORLD SCIENTIFIC. https://doi.org/10.1142/9789814282475_0032

Chu, A., Wang, Z. B., & Vriend, H. de. (2015). Analysis on Residual Coarse Sediment Transport in Estuaries. *Estuarine Coastal and Shelf Science*, *163*, 194–205. https://doi.org/10/gmw236

Chu, A., Wang, Z., Vriend, H. J. de, & Tai, J. (2018). Parallel Morphodynamic Modelling for the Yangtze Estuary. *Journal of Coastal Research*, *85*, 641–645. https://doi.org/10.2112/SI85-129.1

Chu, A., Tai, J., Chen, Y., & Wang, B. (2020). Sediment Budget of the Mouth Bar in the Yangtze Estuary Response to the Change of Marine Input Conditions: A Process-Based Model Approach. *Journal of Coastal Research*, *105*(sp1). https://doi.org/10.2112/JCR-SI105-008.1

Cook, S. E., Warner, J. C., & Russell, K. L. (2023). A numerical investigation of the mechanisms controlling salt intrusion in the delaware bay estuary. *Estuarine, Coastal and Shelf Science*, *283*, 108257. https://doi.org/10.1016/j.ecss.2023.108257

Dai, R., & Zhu, J. (2015). Statistical analysis of the wind at the chongming eastern beach. *Journal of East China Normal University(Natural Science)*, *2015*(4), 17. https://doi.org/10.3969/j.issn.1000-5641.2015.04.003

Geyer, W. R., & MacCready, P. (2014). The Estuarine Circulation. *Annual Review of Fluid Mechanics*, *46*(1), 175–197. https://doi.org/10/gf8f36

Giddings, S. N., & MacCready, P. (2017). Reverse Estuarine Circulation Due to Local and Remote Wind Forcing, Enhanced by the Presence of Along-Coast Estuaries. *Journal of Geophysical Research-Oceans*, *122*(12), 10184–10205. https://doi.org/10/gcv7vh

Gong, W., Chen, Y., Zhang, H., & Chen, Z. (2018). Effects of wave–current interaction on salt intrusion during a typhoon event in a highly stratified estuary. *Estuaries and Coasts*, *41*(7), 1904–1923. https://doi.org/10.1007/s12237-018-0393-8

Hansen D. V., & Rattray M. (1965). Gravitational circulation in straits and estuaries. *J MAR RES*, *23*((2)), 104–122.

Hersbach, H., Bell, B., Berrisford, P., Biavati, G., Horányi, A., Muñoz Sabater, J., et al. (2018). ERA5 hourly data on single levels from 1940 to present [Data set]. Copernicus Climate Change Service (C3S) Climate Data Store (CDS). https://doi.org/10.24381/CDS.ADBB2D47

Hsu, T.-J., Elgar, S., & Guza, R. T. (2006). Wave-induced sediment transport and onshore sandbar migration. *Coastal Engineering*, *53*(10), 817–824. https://doi.org/10.1016/j.coastaleng.2006.04.003

Jongbloed, H., Schuttelaars, H. M., Dijkstra, Y. M., Donkers, P. B., & Hoitink, A. J. F. (2022). Influence of wind on subtidal salt intrusion and stratification in well-mixed and partially stratified estuaries. *Journal of Physical Oceanography*, *52*(12), 3139–3158. https://doi.org/10.1175/JPO-D-21-0291.1

Juárez, B., Ruiz de Alegría-Arzaburu, A., & García-Walther, J. (2024). Tidal, density and wind-driven subtidal circulation in a hypersaline coastal lagoon. *Estuarine, Coastal and Shelf Science*, *301*, 108748. https://doi.org/10.1016/j.ecss.2024.108748

Kalhoro, N. A., He, Z., Li, L., Xu, D., Jun, W., Zeb, A., & Khaskheli, N. (2021). Spatial and temporal variations of hydrodynamics and sediment dynamics in indus river estuary, pakistan. *Global Nest Journal*, *23*(4), 572–580. https://doi.org/10.30955/gnj.003333

Kim, C.-K., & Park, K. (2012). A modeling study of water and salt exchange for a micro-tidal, stratified northern gulf of mexico estuary. *Journal of Marine Systems*, *96–97*, 103–115. https://doi.org/10.1016/j.jmarsys.2012.02.008

Lee, J., Biemond, B., de Swart, H., & Dijkstra, H. A. (2024). Increasing risks of extreme salt intrusion events across european estuaries in a warming climate. *Communications Earth & Environment*, *5*(1), 1–7. https://doi.org/10.1038/s43247-024-01225-w

Lerczak, J. A., Geyer, W. R., & Chant, R. J. (2006). Mechanisms Driving the Time-Dependent Salt Flux in a Partially Stratified Estuary*. *Journal of Physical Oceanography*, *36*(12), 2296–2311. https://doi.org/10.1175/JPO2959.1

Li, Linjiang, Zhu, J., Chant, R. J., Wang, C., & Pareja-Roman, L. F. (2020). Effect of dikes on saltwater intrusion under various wind conditions in the changjiang estuary. *Journal of Geophysical Research: Oceans*, *125*(7), e2019JC015685. https://doi.org/10.1029/2019JC015685

Li, Linjiang, Wang, C., Pareja-Roman, L. F., Zhu, J., Chant, R. J., & Wang, G. (2022). Effects of typhoon on saltwater intrusion in a high discharge estuary. *Journal of Geophysical Research: Oceans*, *127*(8), e2021JC018206. https://doi.org/10.1029/2021JC018206

Li, Lu, Zhu, J., & Wu, H. (2012). Impacts of wind stress on saltwater intrusion in the yangtze estuary. *Science China Earth Sciences*, *55*(7), 1178–1192. https://doi.org/10.1007/s11430-011-4311-1

Longuet-Higgins, M. S., & Stewart, R. w. (1964). Radiation stresses in water waves; a physical discussion, with applications. *Deep Sea Research and Oceanographic Abstracts*, *11*(4), 529–562. https://doi.org/10.1016/0011-7471(64)90001-4

MacCready, P., Geyer, W. R., & Burchard, H. (2018). Estuarine exchange flow is related to mixing through the salinity variance budget. *Journal of Physical Oceanography*, *48*(6), 1375–1384. https://doi.org/10.1175/JPO-D-17-0266.1

Mai, Y., Peng, S., Lai, Z., & Wang, X. (2022). Saltwater intrusion affecting NO2− accumulation in demersal fishery species by bacterially mediated N-cycling. *Science of the Total Environment*, *827*, 154371. https://doi.org/10.1016/j.scitotenv.2022.154371

Mellor, G. L. (2008). The depth-dependent current and wave interaction equations: A revision. *Journal of Physical Oceanography*, *38*(11), 2587–2596. https://doi.org/10.1175/2008JPO3971.1

Monismith, S. G., Kimmerer, W., Burau, J. R., & Stacey, M. T. (2002). Structure and flow-induced variability of the subtidal salinity field in northern san francisco bay. *Journal of Physical Oceanography*, *32*(11), 3003–3019. https://doi.org/10.1175/1520-0485(2002)0322.0.CO

National Marine Data Center. (1999). Observation data in Chinese oceanic stations [Data set]. Retrieved from https://mds.nmdis.org.cn/pages/dataViewDetail.html?dataSetId=4

Pang, C., Zhao, E., & Yang, Y. (2010). Numerical simulation on the process of saltwater intrusion and its impact on the suspended sediment concentration in the changjiang (yangtze) estuary. *Chinese Journal of Oceanology and Limnology*, *28*(3), 609–619. https://doi.org/10.1007/s00343-010-9254-4

Pareja-Roman, L. F., Chant, R. J., & Ralston, D. K. (2019). Effects of locally generated wind waves on the momentum budget and subtidal exchange in a coastal plain estuary. *Journal of Geophysical Research: Oceans*, *124*(2), 1005–1028. https://doi.org/10.1029/2018JC014585

Pfeiffer-Herbert, A. S., Kincaid, C. R., Bergondo, D. L., & Pockalny, R. A. (2015). Dynamics of wind-driven estuarine-shelf exchange in the narragansett bay estuary. *Continental Shelf Research*, *105*, 42–59. https://doi.org/10.1016/j.csr.2015.06.003

Prandle, D. (1981). Salinity intrusion in estuaries. *Journal of Physical Oceanography*, *11*(10), 1311–1324. https://doi.org/10.1175/1520-0485(1981)011<1311:SIIE>2.0.CO;2

Pritchard, D. (1952). Salinity distribution and circulation in the chesapeake bay estuarine system. *Journal of Marine Research*, *11*(2), 106–123.

Qiu, C., Zhu, J., & Gu, Y. (2012). Impact of seasonal tide variation on saltwater intrusion in the changjiang river estuary. *Chinese Journal of Oceanology and Limnology*, *30*(2), 342–351. https://doi.org/10.1007/s00343-012-1115-x

Ross, A. C., Najjar, R. G., Li, M., Mann, M. E., Ford, S. E., & Katz, B. (2015). Sea-level rise and other influences on decadal-scale salinity variability in a coastal plain estuary. *Estuarine, Coastal and Shelf Science*, *157*, 79–92. https://doi.org/10.1016/j.ecss.2015.01.022

Savenije, H. H. G. (2015). Prediction in ungauged estuaries: an integrated theory. *Water Resources Research*, *51*(4), 2464–2476. https://doi.org/10.1002/2015WR016936

Scully, M. E., Friedrichs, C., & Brubaker, J. (2005). Control of estuarine stratification and mixing by wind-induced straining of the estuarine density field. *Estuaries*, *28*(3), 321–326. https://doi.org/10.1007/BF02693915

Simpson, J. H., Brown, J., Matthews, J., & Allen, G. (1990). Tidal straining, density currents, and stirring in the control of estuarine stratification. *Estuaries*, *13*(2), 125. https://doi.org/10.2307/1351581

Tao, Z., Chu, A., Chen, Y., Lu, S., & Wang, B. (2020). Wind effect on the saltwater intrusion in the yangtze estuary. *Journal of Coastal Research*, *105*(sp1). https://doi.org/10.2112/JCR-SI105-009.1

Wang, Jie, Kuang, C., Chen, K., Fan, D., Qin, R., & Han, X. (2022). Wave–current interaction by typhoon fongwong on saline water intrusion and vertical stratification in the yangtze river estuary. *Estuarine, Coastal and Shelf Science*, *279*, 108138. https://doi.org/10.1016/j.ecss.2022.108138

Wang, Jinhua, Zhang, D., Zhang, W., & Zhang, J. (2019). Impacts of different dynamic factors on the saltwater intrusion in the northern branch of the yangtze estuary. *China Ocean Engineering*, *33*(6), 673–684. https://doi.org/10.1007/s13344-019-0065-x

Wang, T., & Geyer, W. R. (2018). The balance of salinity variance in a partially stratified estuary: implications for exchange flow, mixing, and stratification. *Journal of Physical Oceanography*, *48*(12), 2887–2899. https://doi.org/10.1175/JPO-D-18-0032.1

Willmott, C. J. (1981). On the Validation of Models. *Physical Geography*, *2*(2), 184–194. https://doi.org/10.1080/02723646.1981.10642213

Wu, H. (2010). Links between saltwater intrusion and subtidal circulation in the Changjiang Estuary A model-guided study. *Continental Shelf Research*, 15. https://doi.org/10.1016/j.csr.2010.09.001

Xu, Z., Ma, J., Wang, H., & Zhao, J. (2020). Influence of river discharge on the transport of the saltwater group from the north branch in the yangtze river estuary. *International Journal of Environmental Research and Public Health*, *17*(24), 9156. https://doi.org/10.3390/ijerph17249156

Yang, J., Jiang, S., Wu, J., Xie, L., Zhang, S., & Bai, P. (2020). Effects of wave-current interaction on the waves, cold-water mass and transport of diluted water in the Beibu Gulf. *Acta Oceanologica Sinica*, *39*(1), 25–40. https://doi.org/10.1007/s13131-019-1529-9

Zhang, E., Gao, S., Savenije, H. H. G., Si, C., & Cao, S. (2019). Saline water intrusion in relation to strong winds during winter cold outbreaks: north branch of the yangtze estuary. *Journal of Hydrology*, *574*, 1099–1109. https://doi.org/10.1016/j.jhydrol.2019.04.096

Zhang, G., Chen, Y., Cheng, W., Zhang, H., & Gong, W. (2021). Wave effects on sediment transport and entrapment in a channel-shoal estuary: the pearl river estuary in the dry winter season. *Journal of Geophysical Research: Oceans*, *126*(4), e2020JC016905. https://doi.org/10.1029/2020JC016905

Zhang, H., Hu, S., Cheng, W., Zhu, L., Chen, Y., Liu, J., et al. (2021). Response of freshwater transport during typhoons with wave-induced mixing effects in the pearl river estuary, china. *Estuarine, Coastal and Shelf Science*, *258*, 107439. https://doi.org/10.1016/j.ecss.2021.107439

Zhang, Z., Wu, H., Yin, X., & Qiao, F. (2018). Dynamical response of changjiang river plume to a severe typhoon with the surface wave-induced mixing. *Journal of Geophysical Research: Oceans*, *123*(12), 9369–9388. https://doi.org/10.1029/2018JC014266

Zhao, L., Xin, P., Cheng, H., & Chu, A. (2023). Change of turbidity maximum in yangtze estuary after construction of the three gorges dam. *Continental Shelf Research*, *258*, 104983. https://doi.org/10.1016/j.csr.2023.104983

Zhu, C., Van Maren, D. S., Guo, L., Lin, J., He, Q., & Wang, Z. B. (2021). Effects of sediment-induced density gradients on the estuarine turbidity maximum in the yangtze estuary. *Journal of Geophysical Research: Oceans*, *126*(5), e2020JC016927. https://doi.org/10.1029/2020JC016927

Zhu, C., Van Maren, D. S., Guo, L., Lin, J., He, Q., & Wang, Z. B. (2022). Feedback effects of sediment suspensions on transport mechanisms in an estuarine turbidity maximum. *Journal of Geophysical Research: Oceans*, *127*(6), e2021JC018029. https://doi.org/10.1029/2021JC018029

Zhu, J., Cheng, X., Li, L., Wu, H., Gu, J., & Lyu, H. (2020). Dynamic mechanism of an extremely severe saltwater intrusion in the changjiang estuary in february 2014. *Hydrology and Earth System Sciences*, *24*(10), 5043–5056. https://doi.org/10.5194/hess-24-5043-2020